Report

Current Biology

# Actin-Network Architecture Regulates Microtubule Dynamics

## Highlights

- Branched actin networks block microtubule growth and trigger their disassembly
- Unbranched actin networks do not interfere with microtubule growth
- Branched actin networks perturb meiotic spindle assembly in *Xenopus egg* extracts

## Authors

Alexandra Colin, Pavithra Singaravelu, Manuel Théry, Laurent Blanchoin, Zoher Gueroui

## Correspondence

laurent.blanchoin@cea.fr (L.B.), zoher.gueroui@ens.fr (Z.G.)

## In Brief

Colin et al. show that branched actin networks block microtubule growth and trigger microtubule disassembly using *Xenopus* egg extracts and *in vitro* reconstituted systems. This demonstrates the role of actin-network architecture in regulating microtubule dynamics.

Colin et al., 2018, Current Biology *28*, 1–10
August 20, 2018 
https://doi.org/10.1016/j.cub.2018.06.028

CellPress

Please cite this article in press as: Colin et al., Actin-Network Architecture Regulates Microtubule Dynamics, Current Biology (2018), https://doi.org/10.1016/j.cub.2018.06.028

Current Biology
Report

# Actin-Network Architecture Regulates Microtubule Dynamics

Alexandra Colin,[1,4] Pavithra Singaravelu,[2,4] Manuel Théry,[2,3] Laurent Blanchoin,[2,3,*] and Zoher Gueroui[1,5,*]
[1]PASTEUR, Department of Chemistry, École Normale Supérieure, PSL University, Sorbonne Université, CNRS, 75005 Paris, France
[2]Université Grenoble-Alpes, CEA, CNRS, INRA, Biosciences & Biotechnology Institute of Grenoble, Laboratoire de Physiologie Cellulaire & Végétale, CytoMorpho Lab, 17 rue des Martyrs, 38054 Grenoble, France
[3]Université Paris Diderot, INSERM, CEA, Hôpital Saint Louis, Institut Universitaire d'Hematologie, UMRS1160, CytoMorpho Lab, 1 Avenue Claude Vellefaux, 75010 Paris, France
[4]These authors contributed equally
[5]Lead Contact
*Correspondence: laurent.blanchoin@cea.fr (L.B.), zoher.gueroui@ens.fr (Z.G.)
https://doi.org/10.1016/j.cub.2018.06.028

## SUMMARY

Coordination between actin filaments and microtubules is critical to complete important steps during cell division. For instance, cytoplasmic actin filament dynamics play an active role in the off-center positioning of the spindle during metaphase I in mouse oocytes [1–3] or in gathering the chromosomes to ensure proper spindle formation in starfish oocytes [4, 5], whereas cortical actin filaments control spindle rotation and positioning in adherent cells or in mouse oocytes [6–9]. Several molecular effectors have been found to facilitate anchoring between the meiotic spindle and the cortical actin [10–14]. *In vitro* reconstitutions have provided detailed insights in the biochemical and physical interactions between microtubules and actin filaments [15–20]. Yet how actin meshwork architecture affects microtubule dynamics is still unclear. Here, we reconstituted microtubule aster in the presence of a meshwork of actin filaments using confined actin-intact *Xenopus* egg extracts. We found that actin filament branching reduces the lengths and growth rates of microtubules and constrains the mobility of microtubule asters. By reconstituting the interaction between dynamic actin filaments and microtubules in a minimal system based on purified proteins, we found that the branching of actin filaments is sufficient to block microtubule growth and trigger microtubule disassembly. In a further exploration of *Xenopus* egg extracts, we found that dense and static branched actin meshwork perturbs monopolar spindle assembly by constraining the motion of the spindle pole. Interestingly, monopolar spindle assembly was not constrained in conditions supporting dynamic meshwork rearrangements. We propose that branched actin filament meshwork provides physical barriers that limit microtubule growth.

## RESULTS

### Microtubule Aster Assembly in a Cytoplasmic Actin Filament Meshwork

*Xenopus* egg extracts provide a powerful model system to explore the general principles by which microtubule assembly is regulated during metaphase spindle organization [21–24]. However, until now, this cell-free system has been mainly used to study isolated spindle assemblies comprising microtubules but devoid of actin filament structures. To examine the interplay between cytoplasmic actin filament structures and microtubule self-organization, we used *Xenopus laevis* egg extracts with actin filaments intact (actin cytostatic-factor extracts, hereafter referred to as actin-CSF), which correspond to metaphase-II-arrested extracts that have been prepared without inhibiting the growth of endogenous actin filaments [25, 26] (STAR Methods). These actin-CSF extracts were dispersed in mineral oil to generate spherical droplets ranging from a few micrometers up to 100 μm in size, with rigid boundaries (STAR Methods), a size range that was well suited for quantitatively studying the effect of spatial confinement on actin [27, 28] or on microtubule and spindle self-organization [29–31].

To reconstitute actin filament meshworks in the droplets of actin-CSF extract, a nucleation-promoting factor, Scar-PWA (poly-proline rich, WH2 and acidic motifs of Wiskott-Aldrich syndrome protein-WASp; an activator of the Arp2/3 complex), was added to trigger the nucleation of branched actin filaments (STAR Methods). In the absence of PWA, a highly contractile meshwork formed within a droplet that eventually assembled into a ring structure [20, 27] (Figure S1A, left; Video S1). With 250 nM PWA, a sparse and contractile branched meshwork formed homogeneously throughout a droplet (Figures S1A, middle, and S1B; Video S1), with an average contractile rate of 30 $nm.s^{-1}$ (Figure S1C, green data; Video S1). Increasing the PWA concentration to 1.3 μM generated a dense and non-contractile branched meshwork (i.e., a dense and static branched meshwork; Figures S1A, right, and S1C, gray data; Video S1). Multiple particle-tracking experiments of nanoparticles (110 nm) showed that the dense and non-contractile branched meshwork displayed the same viscous properties at the micron scale as a sparse and contractile branched

meshwork. However, and in contrast to the sparse and contractile branched meshwork, nanoparticle trajectories exhibited a more confined motion (with an apparent confinement size of 2.1 and 2.8 μm, respectively; Figure S1D). Therefore, the connectivity of the dense branched meshwork appeared too high to favor myosin-induced contraction, in contrast to what was previously reported [32].

In this egg-extract model, the actin filament meshwork assembled much faster than microtubule structures. Therefore, we explored the effect of pre-assembled actin filament meshwork on the formation of microtubule asters. During spindle formation, asters of microtubules can nucleate at centrosome sites or can assemble in the vicinity of the chromosomes using spindle assembly factors, which are regulated by a Ran-dependent pathway [33]. Here, a constitutively active form of RanGTP, chromosomes (from sperm nuclei), or centrosomes was used to promote aster assembly in actin-CSF droplets.

Aster assembly was monitored in absence of actin filaments (using actin-CSF extracts treated with latrunculin A, an actin filament depolymerizing agent, and blebbistatin, a myosin II inhibitor) and, in the presence of actin filaments, either with a sparse and contractile branched meshwork or a dense and non-contractile branched meshwork (Figure 1A). Microtubules were visualized using fluorescein isothiocyanate (FITC)-tubulin, tetramethylrhodamine (TRITC)-tubulin, or EB1-GFP, and actin filaments were visualized using dsRed-utrophin or GFP-utrophin.

In the first set of experiments, microtubule structures were primarily induced by adding RanQ69L (constitutively active RanGTP; STAR Methods). In the absence of actin filaments, the asters that assembled contained radial arrays of microtubules with an average length of 10.8 ± 5.5 μm (Figures 1C and 1D; STAR Methods). In presence of a branched actin meshwork, microtubules organized into morphologically similar asters to those observed in absence of actin filaments (Figure 1A). Actin filaments co-aligned with microtubules, reflecting the remodeling of actin filaments into aster-like organizations (Figure 1B). In comparison with the absence of actin filaments, the average lengths of microtubules were lower with the sparse and contractile actin meshwork at 8.8 μm (19% reduction; Figure 1D, green) and with the dense and static actin meshwork at 7.8 μm (27% reduction; Figure 1D, gray). This was confirmed by evaluating the EB1 density as function of the distance from the aster center (STAR Methods; Figure S2A).

Microtubule length was also correlated with microtubule growth rate in both static and contractile meshworks (Figures 1D and 1E, left; STAR Methods). This correlation appeared independent of a direct effect of PWA on microtubule dynamics because, in the absence of actin filaments, the average microtubule growth rate of 16.6 $\mu m.min^{-1}$ with 1.3 μM PWA added (Figure S2B) was not significantly different to 17.8 $\mu m.min^{-1}$ without PWA added. The reduction of microtubule dynamics appeared not to be due to the reduction of ATP availability in the droplets. No significant differences in microtubule growth rates were identified in asters nucleated from chromosomes at early and late time periods (30 and 60 min after droplet formation; Figure S2C). Altogether, these data suggest that the microtubule growth in asters was perturbed by the degree of branching within the actin meshworks and that this perturbation was not dependent on actin contractility.

In a second set of experiments, microtubule structures were induced by adding centrosomes to the actin-CSF extracts. As with the asters induced by constitutively active Ran, actin filaments and radial microtubules also co-aligned in centrosome-induced asters (Figure 1B). In comparison with the condition in which an actin filament meshwork was absent, microtubule length and growth rate were reduced on average by about 19% and 30%, respectively, in the presence of sparse and contractile branched actin meshwork (Figures 1D, 1E, and S2A). Microtubule length and growth rate were also lower in the presence of a dense and static branched actin meshwork. Therefore, similar effects of branched actin meshworks on microtubule lengths and dynamics were observed with asters induced by centrosomes to those asters induced by constitutively active Ran GTP.

We have shown previously that centrosomes can directly promote actin filament assembly [34]. Therefore, we assessed whether centrosomes can elongate actin filaments and promote aster-like structures of actin filaments independently from promoting microtubule asters in the actin-CSF extract. When centrosomes were incubated in a dense actin filament meshwork and in presence of nocodazole to prevent microtubule formation, no aster-like structures of actin filaments were observed. Centrosomes appeared entrapped within the actin filament meshwork, surrounded by points of high actin densities (Figure S2D). In addition, no actin filaments were observed to emanate from microtubule templates. Therefore, these data suggest that aster-like organizations of actin filaments resulted from the alignment of pre-assembled actin filaments along microtubules.

To assess the effect of meshwork density on actin filament alignment with microtubules, we obtained a new meshwork by adding 4 μM of latrunculin A and 250 nM PWA to the actin-CSF extract. This meshwork, hereafter referred to as a loose meshwork, was less dense than the meshwork described above. With this loose meshwork, actin filaments reorganized around the microtubules at the aster pole (Figure S2E). In addition, the average growth rate of microtubules nucleated using RanQ69L was as expected (Figure S2F; 13.1 $\mu m.min^{-1}$) in being intermediate between those average growth rates of microtubules nucleated in absence of actin filaments (17.8 $\mu m.min^{-1}$) and microtubules nucleated in a sparse and contractile branched meshwork (11.3 $\mu m.min^{-1}$).

## Microtubule Length and Dynamics Depend on Actin Filament Branching *In Vitro*

To have more insights on the role of actin assembly on microtubule dynamics and bypass the complexity of the egg-extract model, we studied the effect of different actin architectures (branched or unbranched meshwork) on microtubule dynamics using reconstituted systems based on purified proteins (Figure 2). The dynamics of actin filaments and microtubules were maintained by use of the TicTac buffer [34]. Growth of microtubules was initiated from biotinylated, non-hydrolysable, and stabilized microtubule seeds attached to the substrate surface by addition of 25 μM of labeled tubulin in presence of labeled actin monomers alone (unbranched meshwork) or with the Arp2/3 complex activated by WASP-WA (WH2 and acidic motifs of Wiskott-Aldrich syndrome protein-WASp; branched meshwork). The behavior of individual actin filaments and microtubules were

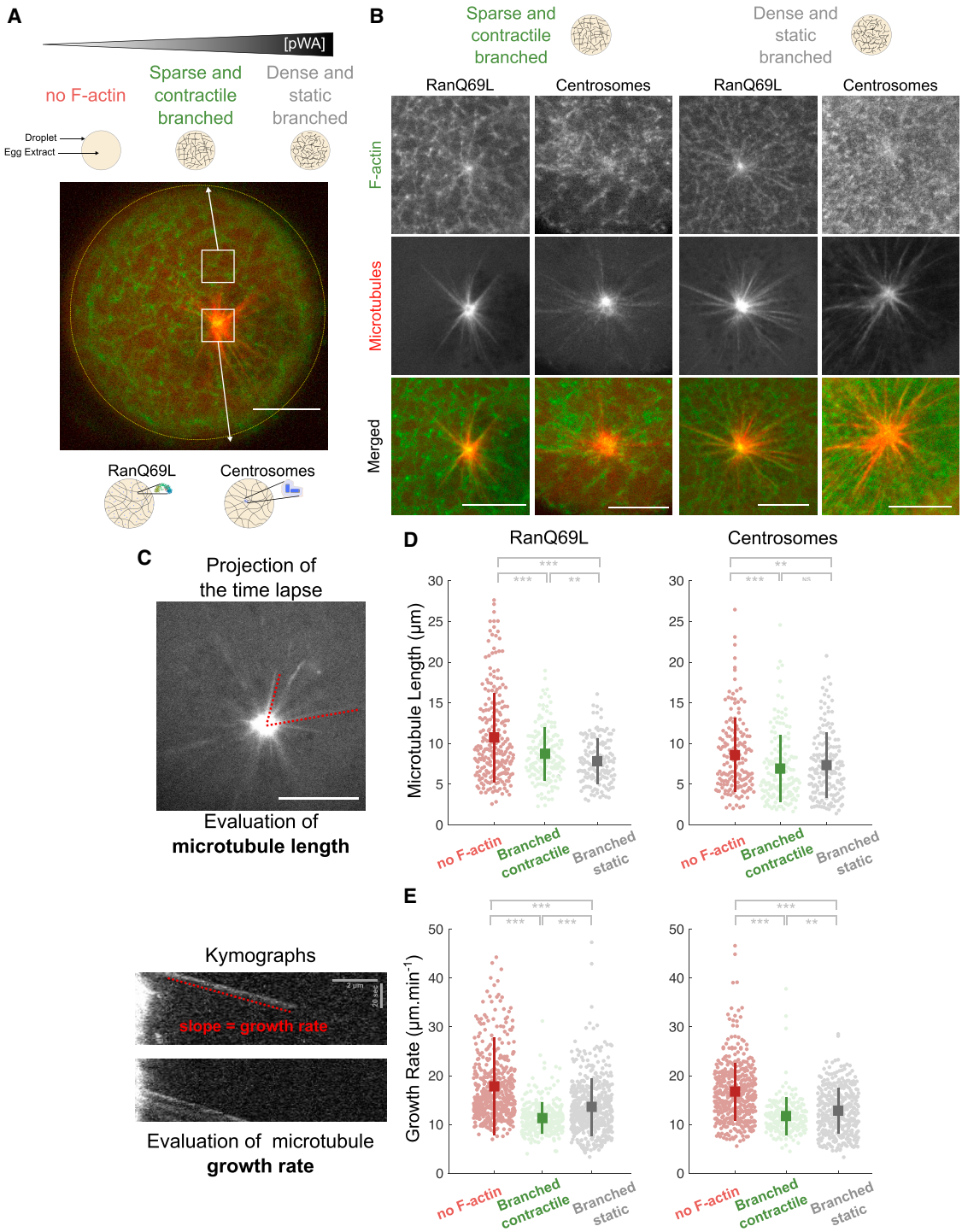


**Figure 1. Microtubule Aster Assembly in a Cytoplasmic Actin Filament Meshwork**

(A) The principle of the experiment: the monitoring of microtubule formation in absence of actin filaments (extracts treated with latrunculin A and blebbistatin), in a sparse and contractile branched meshwork, or in dense and static branched meshwork. Asters were formed from two nucleation pathways: RanQ69L or centrosomes. Actin filaments were labeled with GFP-utrophin and microtubules with TRITC-tubulin. The scale bar represents 10 µm.

(B) Ran and centrosome-nucleated asters in sparse and contractile branched or dense and static branched actin meshwork. Actin filaments are labeled with GFP-utrophin and microtubules with TRITC-tubulin. The scale bars represent 10 µm.

(C) Microtubule length was evaluated by measuring EB1 traces. Growth rates were evaluated from kymographs (STAR Methods). The scale bar represents 10 µm.

(D and E) Quantitative analysis of microtubule length (D) and growth rate (E) for RanQ69L and centrosome-nucleated asters in various actin filament meshworks. Each point represents a single measurement for one microtubule. Means and SDs are superimposed. $^{**}p < 0.01$, $^{***}p < 0.001$.

See also Figures S1 and S2 and Video S1.

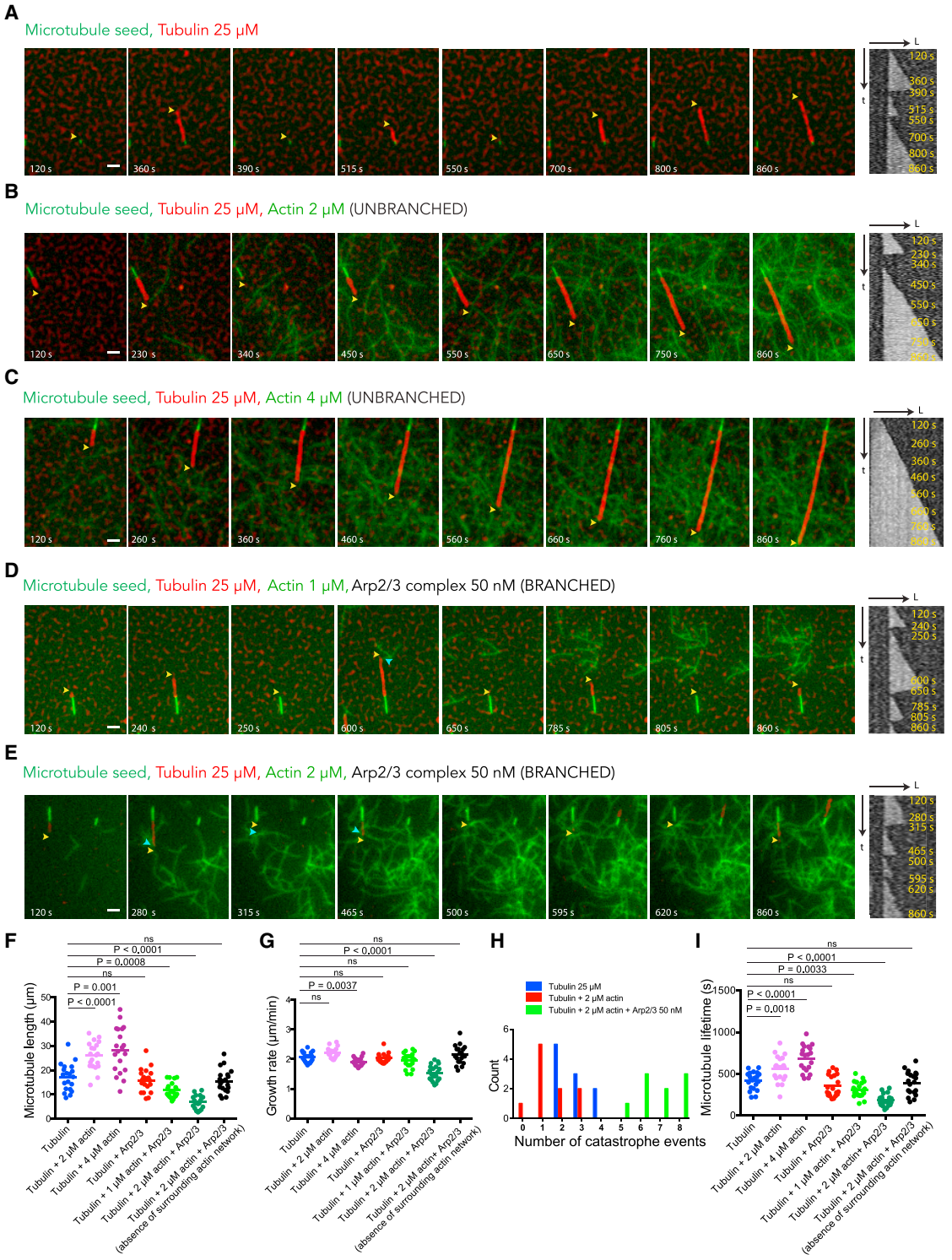


**Figure 2. Actin Architectures Modulate Microtubule Dynamics**

(A) Time-lapse of *in vitro* reconstitution of microtubules (red) growing from biotinylated GMPCPP-stabilized microtubule seeds (green) at 25 μM tubulin concentration. Kymograph highlighting the time points of growth and catastrophe events acquired during the Video S2 is shown.

(B) Trajectories of microtubule growth (red) at 25 μM tubulin in the presence of unbranched actin network—green (2 μM). Microtubule seeds are also shown in green. Kymograph corresponding to the Video S2 is shown.

(C) Trajectories of microtubule growth (red) at 25 μM tubulin in the presence of unbranched actin network—green (4 μM). Microtubule seeds are also shown in green. Kymograph corresponding to the Video S2 is shown.

*(legend continued on next page)*

monitored by total internal reflection fluorescence (TIRF) microscopy.

In the absence of actin filaments, microtubules exhibit the characteristic alternate phases of growth and catastrophe (Figure 2A; Video S2). In comparison, and in the presence of unbranched actin meshwork (2 μM actin), the apparent microtubule growth rate was similar (2.2 ± 0.2 $\mu m.min^{-1}$ versus 2.1 ± 0.2 $\mu m.min^{-1}$), and the catastrophes were slightly less frequent, resulting in a slightly higher microtubule length (25.9 ± 5.7 μm versus 17.1 ± 5.6 μm; Figures 2B, 2F, 2G, and 2I; Video S2). Increasing the density of unbranched actin meshwork (4 μM actin) further stabilized microtubule growth, resulting in an average length of 28.3 ± 9.3 μm (Figures 2C, 2F, 2G, and 2I; Video S2). By contrast, in the presence of branched actin meshwork (1 μM actin +Arp2/3), the microtubule length was significantly lower (11.8 ± 3.2 μm) in comparison to the condition without actin filaments (Figures 2D, 2F, 2G, and 2I; Video S2). Increasing the density of branched actin meshwork (2 μM actin +Arp2/3) further decreased both the microtubule growth rate (1.5 ± 0.3 $\mu m.min^{-1}$) and microtubule length (6.8 ± 2.7 μm; Figures 2E, 2F, 2G, and 2I; Video S2). Also, microtubule catastrophes were significantly more frequent (Figure 2H). Catastrophe events typically occurred (Figure 2E; Video S2) when microtubule growing plus ends (yellow arrows in Figure 2E) encountered a branched actin meshwork (blue arrows in Figure 2E). Hence, the average lifetime of microtubules was also significantly lower in comparison to the condition without actin filaments (181.8 ± 68.6 s versus ~418 ± 107.6 s; Figure 2I). Our data revealed that the architecture (branched versus unbranched) is the key determinant in affecting microtubule dynamics. Interestingly, increasing actin density has an opposite effect on microtubule dynamics, depending on the actin architecture. Microtubules are stabilized by the unbranched meshwork whereas destabilized by the branched meshwork (Figures 2F and 2I). Moreover, these significant effects on microtubule dynamics appeared independent of the direct activity of actin monomers and the Arp2/3 complex on microtubules because the dynamics of microtubules that were not in direct contact with the branched actin network were not significantly different from those observed in the condition without actin filaments. These data generated at the resolution of single filaments indicate that actin filament branching appears sufficient to perturb microtubule elongation, which is consistent with the role of the Arp2/3 complex on microtubule growth in the egg-extract model.

## Aster Mobility Is Severely Restricted in Actin Filament Meshwork

To assess whether actin filament meshworks could act as a physical barrier by constraining and trapping the microtubule asters in an elastic gel, we monitored the motion of microtubule asters induced by constitutively active Ran in the egg-extract model. The mobility of asters is likely to be driven by pushing and pulling forces generated by the microtubules [29, 35]. Also, the co-localization of actin filaments with aster poles (as previously observed) [15, 33] suggests a strong enrichment of actin surrounding the pole (Figure 1B).

In the absence of actin filaments, the aster poles were very dynamic and moved throughout large parts of the droplet space (Figure 3A, left; Video S3). By contrast, in the presence of either sparse-contractile or dense-static branched-actin meshworks, the motion of aster poles was much more limited (Figure 3A, middle and right; Video S3) and confirmed by lower mean square displacement (MSD) values that capture the surface areas covered by the aster poles (Figure 3B).

In the presence of a loose meshwork (PWA + latrunculin A), the motion of aster poles was intermediate between that observed with the absence of actin filaments (red curve, Figure 3B) and the presence of a sparse contractile or dense static branched meshwork (green and gray curves, Figure 3B), indicating an inverse correlation between actin filament branching density and aster-pole mobility. Interestingly, in the presence of the sparse branched meshwork, the contractile velocity of the actin (11.0 $nm.s^{-1}$) was similar to the aster speed (10.8 $nm.s^{-1}$; Figure 3C; Video S4). These data indicated that a branched meshwork constrained the mobility of the microtubule aster and potentially modulated aster mobility through its contractile activity.

## Monopolar Spindle Formation in Actin Filament-Intact Egg Extracts Confined in Droplets

To assess the effects of actin filament architecture and dynamics on spindle formation in actin-CSF extracts, we used sperm nuclei (hereafter referred to as chromosomes), which drive the formation of meiotic monopolar spindles in conventional CSF extracts [22, 36]. These spindle structures correspond to focused

(D) Trajectories of microtubule growth (red) at 25 μM tubulin in the presence of branched actin network—green (1 μM) produced with 50 nM of the Arp2/3 complex and 120 nM glutathione S-transferase (GST)-WA. Kymograph obtained from Video S2 is shown. Branched actin network is indicated with arrows in blue.
(E) Trajectories of microtubule growth (red) at 25 μM tubulin in the presence of branched actin network—green (2 μM) produced with 50 nM of the Arp2/3 complex and 120 nM GST-WA. The kymograph obtained from Video S2 is shown with more frequent catastrophes compared with the kymographs in the (A) or (B). Branched actin network is indicated with arrows in blue. Microtubule plus ends are indicated with arrows in yellow in (A)–(E). The scale bar represents 20 μm.
(F) Length analysis of microtubules grown *in vitro* from biotinylated GMPCPP-stabilized microtubule seeds in the absence or presence of actin and the Arp2/3 complex. Microtubule length was not affected by the presence or absence of Arp2/3 complex alone; ns, non-significant.
(G) Analysis of growth rate of the microtubules as calculated from their respective kymographs. Slope of the growth phase is expressed as the apparent growth rate in $\mu m.min^{-1}$ along the x axis. Microtubules grown under branched actin network conditions (tubulin + actin + the Arp2/3 complex) display a significantly lower apparent growth rate ($p < 0.0001$).
(H) Analysis of the number of catastrophe events. Microtubules grown in the presence of actin and the Arp2/3 complex display more catastrophic events than in the presence of actin or tubulin alone.
(I) Lifetime distribution of microtubules. Microtubules in the presence of branched actin network (tubulin + actin + the Arp2/3 complex) were the most short lived, with an average lifetime of <200 s compared with the microtubule control (~400 s). Error bars show mean ± SD for n = 20 microtubules per condition, pooled from 3 independent experiments. The p value was generated by Mann-Whitney test, assuming non-paired and non-Gaussian distribution.
(A–E) The scale bars represent 20 μm. See also Video S2.

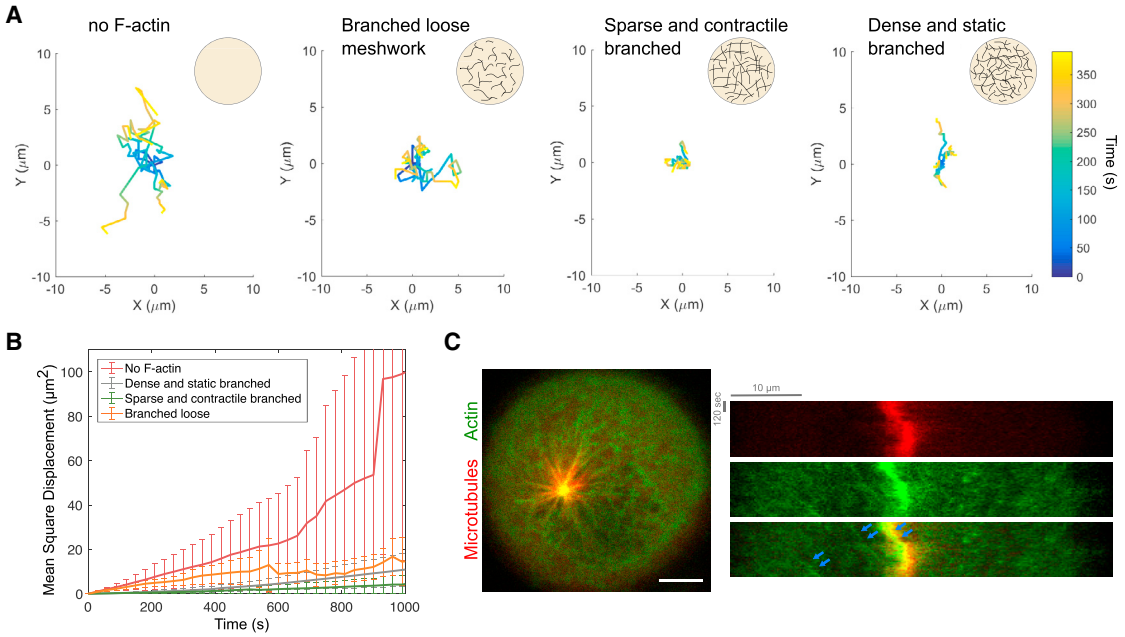


**Figure 3. Aster Pole Mobility in Actin Filament Meshworks with Different Dynamic Properties**

(A) Trajectories of Ran-aster poles nucleated in four different conditions: (1) in absence of actin filaments (extract treated with drugs); (2) in a branched loose meshwork (extract incubated with 250 nM of PWA and 4 μM of latrunculin A); (3) in a sparse and contractile branched meshwork (extract incubated with 250 nM of PWA); and (4) in a dense and static branched meshwork (extract incubated with 1.3 μM of PWA). Normalized trajectories in space are represented, and time is encoded in color.

(B) Quantification of mean square displacements.

(C) Representative kymograph extracted from Video S4, showing that aster pole is transported by the actin filament meshwork contraction. Actin filaments were labeled with GFP-utrophin, and microtubules were labeled with TRITC-tubulin. The scale bar represents 10 μm. Error bars represent SD.

See also Videos S3 and S4.

asters (spindle poles) with microtubules asymmetrically distributed from the pole to the chromosomes. In absence of actin filaments, monopolar spindle organization was characteristic of that obtained in conventional CSF extracts (Figures 4A and S3A). As expected, the nuclear mitotic apparatus protein (NuMA) was localized at the spindle poles (Figure S3B; STAR Methods). Interestingly, the pole-to-chromosome distance was correlated with the droplet diameter (Figure S3C). This was in agreement with previous studies that examined spindle assembly in confined droplets and in *Xenopus* embryogenesis [30, 31], suggesting that spindle size is dictated by the available quantities of certain essential spindle-assembly factors [30, 31, 37].

In the presence of actin filaments, the microtubule structures also acquired a monopolar spindle morphology (Figures 4A, S3D, and S3G). NuMA was localized to the spindle poles, illustrating that NuMA recruitment was unaffected by the actin filament meshwork (Figures S3E and S3H). As observed above with microtubule asters, actin filaments were also organized into aster-like structures at the spindle poles (Figure S4A).

In the presence of a sparse and contractile branched meshwork, the spindles had a pole-to-chromosome distance similar to that observed in the absence of actin filaments (9.3 ± 4 μm in both cases; Figure 4B). By contrast, in the presence of a dense and static branched meshwork, spindle poles formed in closer proximity to the chromosomes with a 35% lower pole-to-chromosome distance (6.1 ± 3 μm), suggesting that spindle formation was arrested earlier in the presence of a dense and static branched meshwork (Figures 4A and 4B).

As with the absence of actin filaments, in the presence of sparse and contractile branched meshwork, the pole-to-chromosome distance was correlated with the droplet diameter (Figure S3F). However, in the presence of dense and static branched meshwork, the pole-to-chromosome distance was not correlated with the droplet diameter (Figure S3I).

Microtubule dynamics were also affected by the dense and static branched meshwork. In the absence of actin filaments or in the presence of a sparse and contractile branched meshwork, microtubule lengths (13 ± 6 μm and 14 ± 7 μm, respectively) and growth rates (17 and 18 $\mu m.min^{-1}$, respectively) were similar (Figure 4C). By contrast, in the presence of a dense and static branched meshwork, the microtubule length was lower by 15% (11 ± 5 μm; Figure 4C) and the growth rate was lower by 23% (13 $\mu m.min^{-1}$). Hence, microtubule growth appeared less perturbed by the presence of an actin filament meshwork when those structures were induced by chromosomes rather than constitutively active Ran or centrosomes. This could be explained by the presence of the RanGTP gradient generated by chromosomes, which is known to favor the local stabilization of growing microtubules in the vicinity of the chromatin [38, 39]. Nevertheless, a dense and static branched meshwork affected monopolar spindle self-organization by primarily perturbing the pole-to-chromosome distance.

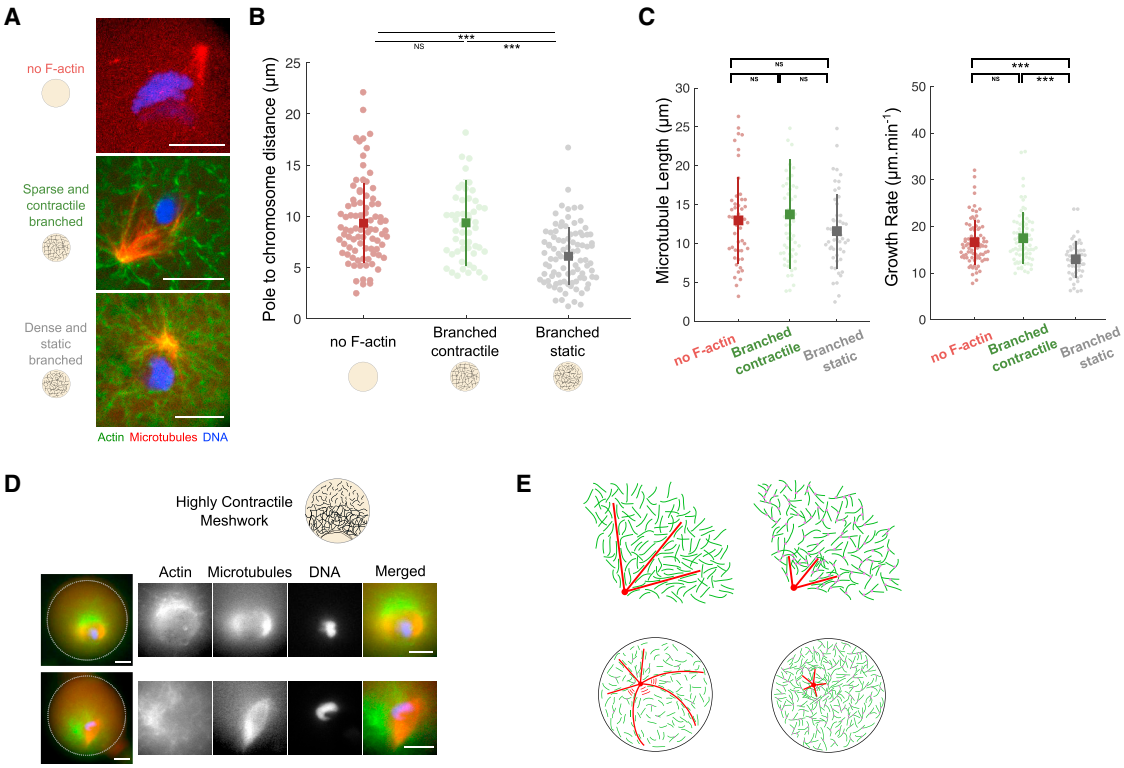


**Figure 4. Aster Spindle Self-Organization in Actin Filament-Intact Egg Extracts Confined in Droplets**

(A) Microtubule self-organization in droplet-confined egg extracts in the absence of actin filaments (extract treated with latrunculin A and blebbistatin), in the presence of a sparse and contractile branched meshwork (250 nM PWA) or in the presence of a dense and static branched meshwork (1.3 μM PWA). The scale bars represent 10 μm.

(B) Pole-to-chromosome distance measured for the three cases described above. Each point represents a single measurement for one microtubule. Means and SDs are superimposed. ***$p < 0.001$.

(C) Length and growth rate of chromosome-nucleated microtubules. The procedure of measurement is the same as described in Figure 1. Each point represents a single measurement for one microtubule. Means and SDs are superimposed. ***$p < 0.001$.

(D) Microtubule nucleation in a highly contractile actin filament meshwork. Chromosomes and microtubules are entrapped in the actin filament ring structure. The scale bar represents 10 μm.

(E) Schematic of the effect of actin filament branching meshwork on microtubule length and aster pole motion.

See also Figures S3 and S4.

In absence of actin filament branching (no PWA added), a highly contractile actin meshwork was formed. This meshwork transported and confined chromosomes within a ring-like structure of actin filaments (Figure 4D). Nevertheless, both monopolar and bipolar spindle structures were induced despite the constraints generated by actin filament architecture and contractility (Figure 4D). In a few cases, microtubules were deformed by actin filaments and actin filaments were deformed by microtubules (Figures S4B and S4C). However, and overall, the actin filaments primarily acted as a geometrical boundary within which chromosomes could still trigger microtubule nucleation.

## DISCUSSION

Our study examined how microtubule assembly and dynamics are affected by the presence and architecture of the network of actin filaments. In *Xenopus* egg extracts, the length and growth rates of microtubules were perturbed in a concentration-dependent manner by branched actin filaments, even though the morphology of the microtubule aster was unaffected. In a reconstituted *in vitro* model based on the minimal composition of proteins necessary to support the dynamic assembly and/or disassembly of both microtubules and actin filaments, branched actin filaments formed an entangled meshwork that could perturb microtubule elongation and trigger microtubule disassembly. Altogether, the results from these two models suggest that branched actin meshwork physically constrains microtubule growth. Microtubule growth has also been shown to be regulated by mechanical forces in *in vitro* assays [40, 41]. Hence, in this study, we propose that branches along actin filaments form reticulation points in a physically interconnected network. The consequential increase in network stiffness acts as an obstacle against growing microtubules and perturbs their polymerization velocity by generating forces opposing microtubule growth (Figure 4E). In addition, the microtubule stabilization by unbranched actin filaments could be due to crowding effect.

Microtubule assembly in spatially confined droplets of *Xenopus* egg extracts provides additional insights on the interplay

between microtubule and the actin filament meshwork. Microtubules tended to locally dictate actin filament geometry by guiding the microfilament organization into aster-like structures (Figures 1B and S4A). This is in agreement with observations showing that microtubule organization can constrain actin filament alignment *in vitro* [15, 18] or *in vivo* [1, 2]. The co-alignments between microtubules and actin filaments are also correlated with a reduction of microtubule growth rate. In this scheme, actin filament density and co-alignment with microtubules could sterically hinder and limit subunit addition at the microtubule plus end. The multiple contacts between microtubules and actin filaments, probably mediated by the presence of cross-linkers, could generate friction forces opposing microtubule growth (Figure 4E). Such mechanical regulation of microtubules by actin filaments may play a role in living cells and complement biochemical regulation of the coordination between actin filaments and microtubules [42, 43]. Hence, the co-alignment of microtubules and actin filaments could also result in a spatial reorganization of biochemical effectors.

Monopolar spindle formation was arrested at an early stage in dense and static branched actin meshwork, whereas it can assemble properly in a sparse and dynamic one. This difference in monopolar spindle formation can be explained by greater stiffness of the dense meshwork versus the sparse meshwork. Indeed, the modulus of elasticity of semi-flexible actin filament meshwork increases with local actin concentration [44] as well as with the degree of branching [45]. In turn, the greater stiffness of the dense meshwork generates a larger resistive force that opposes the force-generating elements driving the outward growth of the spindle pole (Figure 4E). In the sparse meshwork, the resistive force is insufficient to perturb the force-generating elements driving spindle growth.

Actin meshwork density and architecture restricted the mobility of microtubule aster in the egg extracts. This effect is likely to be relevant in the specific regulation of the motion and position of interphase asters or meiotic or mitotic spindles. Actin filament assembly and the mechanical properties of the meshwork have been shown in mouse oocytes to control spindle centering or migration toward the periphery of the oocyte [8, 9]. In addition, actin filaments are essential for the proper alignment and segregation of chromosomes during meiosis because they drive the formation of kinetochore fibers [46]. Moreover, actin filament spatiotemporal dynamics are tightly regulated in cells and oscillate strongly throughout the cell cycle [47, 48].

In conclusion, the temporal and spatial regulation of the dynamics and architecture of networks of actin filaments can impact microtubule network self-organization and positioning via the production of mechanical forces resisting microtubule growth. The resultant physical interactions of actin filaments with microtubules could also result in a spatial reorganization of biochemical effectors regulating both cytoskeletal networks.

## STAR★METHODS

Detailed methods are provided in the online version of this paper and include the following:

- KEY RESOURCES TABLE
- CONTACT FOR REAGENT AND RESOURCE SHARING
- EXPERIMENTAL MODEL AND SUBJECT DETAILS
  - Actin-intact *Xenopus* egg extract preparation
- METHOD DETAILS
  - Protein production and purification
  - Microtubule nucleation and observation in *Xenopus* egg extracts
  - Generation of emulsion droplets/encapsulated extracts
  - Actin nucleation and observation in confined *Xenopus* extracts
  - Bead coating
  - *In vitro* reconstitution of actin and microtubule networks
  - Imaging of Confined *Xenopus* extracts
  - Imaging of actin and microtubule networks *in vitro* by TIRF microscopy
- QUANTIFICATION AND STATISTICAL ANALYSIS
  - Data analysis of Confined *Xenopus* extracts
  - Data analysis of *in vitro* actin and microtubule networks

## SUPPLEMENTAL INFORMATION

Supplemental Information includes four figures and four videos and can be found with this article online at https://doi.org/10.1016/j.cub.2018.06.028.

## ACKNOWLEDGMENTS

We thank Jérémie Gaillard and Christophe Guérin for their invaluable technical help, James Pelletier and Timothy J. Mitchison for providing the antibody NuMA-GFP, and James Sillibourne for providing the purified centrosomes. We thank Marie-Hélène Verlhac and Marie-Emilie Terret for careful reading of the manuscript. We also thank all the members of the "Pole de Chimie Biophysique" and F. Robin for fruitful discussions. A.C. was supported by a "Ministère de la Recherche" predoctoral fellowship. This work was supported by the Centre National de la Recherche Scientifique (CNRS), Ville de Paris "Emergence(s)," Ecole Normale Supérieure, and the Agence Nationale de la recherché (ANR) ReconstMT-Act (ANR-14-CE09-0014-01).

## AUTHOR CONTRIBUTIONS

A.C. performed the experiments with *Xenopus* egg extracts. P.S. performed the experiments with purified actin and tubulin. A.C., M.T., L.B., and Z.G. conceived and analyzed the experiments. A.C., M.T., L.B., and Z.G. wrote the manuscript, and all authors were involved in revising it critically for important intellectual content.

## DECLARATION OF INTERESTS

The authors declare no competing interests.

Received: May 23, 2017
Revised: March 13, 2018
Accepted: June 14, 2018
Published: August 9, 2018

## REFERENCES

1. Azoury, J., Lee, K.W., Georget, V., Rassinier, P., Leader, B., and Verlhac, M.H. (2008). Spindle positioning in mouse oocytes relies on a dynamic meshwork of actin filaments. Curr. Biol. *18*, 1514–1519.
2. Schuh, M., and Ellenberg, J. (2008). A new model for asymmetric spindle positioning in mouse oocytes. Curr. Biol. *18*, 1986–1992.

3. Li, H., Guo, F., Rubinstein, B., and Li, R. (2008). Actin-driven chromosomal motility leads to symmetry breaking in mammalian meiotic oocytes. Nat. Cell Biol. *10*, 1301–1308.
4. Lénárt, P., Bacher, C.P., Daigle, N., Hand, A.R., Eils, R., Terasaki, M., and Ellenberg, J. (2005). A contractile nuclear actin network drives chromosome congression in oocytes. Nature *436*, 812–818.
5. Mori, M., Monnier, N., Daigle, N., Bathe, M., Ellenberg, J., and Lénárt, P. (2011). Intracellular transport by an anchored homogeneously contracting F-actin meshwork. Curr. Biol. *21*, 606–611.
6. Kunda, P., and Baum, B. (2009). The actin cytoskeleton in spindle assembly and positioning. Trends Cell Biol. *19*, 174–179.
7. Morin, X., and Bellaïche, Y. (2011). Mitotic spindle orientation in asymmetric and symmetric cell divisions during animal development. Dev. Cell *21*, 102–119.
8. Chaigne, A., Campillo, C., Gov, N.S., Voituriez, R., Azoury, J., Umaña-Diaz, C., Almonacid, M., Queguiner, I., Nassoy, P., Sykes, C., et al. (2013). A soft cortex is essential for asymmetric spindle positioning in mouse oocytes. Nat. Cell Biol. *15*, 958–966.
9. Chaigne, A., Campillo, C., Voituriez, R., Gov, N.S., Sykes, C., Verlhac, M.-H., and Terret, M.-E. (2016). F-actin mechanics control spindle centring in the mouse zygote. Nat. Commun. *7*, 10253.
10. Rump, A., Scholz, T., Thiel, C., Hartmann, F.K., Uta, P., Hinrichs, M.H., Taft, M.H., and Tsiavaliaris, G. (2011). Myosin-1C associates with microtubules and stabilizes the mitotic spindle during cell division. J. Cell Sci. *124*, 2521–2528.
11. Wu, S.Z., and Bezanilla, M. (2014). Myosin VIII associates with microtubule ends and together with actin plays a role in guiding plant cell division. eLife *3*, 1–20.
12. Weber, K.L., Sokac, A.M., Berg, J.S., Cheney, R.E., and Bement, W.M. (2004). A microtubule-binding myosin required for nuclear anchoring and spindle assembly. Nature *431*, 325–329.
13. Woolner, S., O'Brien, L.L., Wiese, C., and Bement, W.M. (2008). Myosin-10 and actin filaments are essential for mitotic spindle function. J. Cell Biol. *182*, 77–88.
14. Kwon, M., Bagonis, M., Danuser, G., and Pellman, D. (2015). Direct microtubule-binding by myosin-10 orients centrosomes toward retraction fibers and subcortical actin clouds. Dev. Cell *34*, 323–337.
15. Preciado López, M., Huber, F., Grigoriev, I., Steinmetz, M.O., Akhmanova, A., Koenderink, G.H., and Dogterom, M. (2014). Actin-microtubule coordination at growing microtubule ends. Nat. Commun. *5*, 4778.
16. Henty-Ridilla, J.L., Rankova, A., Eskin, J.A., Kenny, K., and Goode, B.L. (2016). Accelerated actin filament polymerization from microtubule plus ends. Science *352*, 1004–1009.
17. Sider, J.R., Mandato, C.A., Weber, K.L., Zandy, A.J., Beach, D., Finst, R.J., Skoble, J., and Bement, W.M. (1999). Direct observation of microtubule-f-actin interaction in cell free lysates. J. Cell Sci. *112*, 1947–1956.
18. Waterman-Storer, C., Duey, D.Y., Weber, K.L., Keech, J., Cheney, R.E., Salmon, E.D., and Bement, W.M. (2000). Microtubules remodel actomyosin networks in Xenopus egg extracts via two mechanisms of F-actin transport. J. Cell Biol. *150*, 361–376.
19. Nguyen, P.A., Groen, A.C., Loose, M., Ishihara, K., Wuhr, M., Field, C.M., and Mitchison, T.J. (2014). Spatial organization of cytokinesis signaling reconstituted in a cell-free system. Science *346*, 244–247.
20. Colin, A., Bonnemay, L., Gayrard, C., Gautier, J., and Gueroui, Z. (2016). Triggering signaling pathways using F-actin self-organization. Sci. Rep. *6*, 34657.
21. Heald, R., Tournebize, R., Blank, T., Sandaltzopoulos, R., Becker, P., Hyman, A., and Karsenti, E. (1996). Self-organization of microtubules into bipolar spindles around artificial chromosomes in Xenopus egg extracts. Nature *382*, 420–425.
22. Mitchison, T.J., Maddox, P., Groen, A., Cameron, L., Perlman, Z., Ohi, R., Desai, A., Salmon, E.D., and Kapoor, T.M. (2004). Bipolarization and poleward flux correlate during Xenopus extract spindle assembly. Mol. Biol. Cell *15*, 5603–5615.
23. Caudron, M., Bunt, G., Bastiaens, P., and Karsenti, E. (2005). Spatial coordination of spindle assembly by chromosome-mediated signaling gradients. Science *309*, 1373–1376.
24. Brugués, J., Nuzzo, V., Mazur, E., and Needleman, D.J. (2012). Nucleation and transport organize microtubules in metaphase spindles. Cell *149*, 554–564.
25. Field, C.M., Nguyen, P.A., Ishihara, K., Groen, A.C., and Mitchison, T.J. (2014). Xenopus egg cytoplasm with intact actin. Methods Enzymol. *540*, 399–415.
26. Field, C.M., Pelletier, J.F., and Mitchison, T.J. (2017). Xenopus extract approaches to studying microtubule organization and signaling in cytokinesis. Methods Cell Biol. *137*, 395–435.
27. Pinot, M., Steiner, V., Dehapiot, B., Yoo, B.-K., Chesnel, F., Blanchoin, L., Kervrann, C., and Gueroui, Z. (2012). Confinement induces actin flow in a meiotic cytoplasm. Proc. Natl. Acad. Sci. USA *109*, 11705–11710.
28. Abu Shah, E., and Keren, K. (2014). Symmetry breaking in reconstituted actin cortices. eLife *3*, e01433.
29. Pinot, M., Chesnel, F., Kubiak, J.Z., Arnal, I., Nedelec, F.J., and Gueroui, Z. (2009). Effects of confinement on the self-organization of microtubules and motors. Curr. Biol. *19*, 954–960.
30. Hazel, J., Krutkramelis, K., Mooney, P., Tomschik, M., Gerow, K., Oakey, J., and Gatlin, J.C. (2013). Changes in cytoplasmic volume are sufficient to drive spindle scaling. Science *342*, 853–856.
31. Good, M.C., Vahey, M.D., Skandarajah, A., Fletcher, D.A., and Heald, R. (2013). Cytoplasmic volume modulates spindle size during embryogenesis. Science *342*, 856–860.
32. Ennomani, H., Letort, G., Guérin, C., Martiel, J.-L., Cao, W., Nédélec, F., De La Cruz, E.M., Théry, M., and Blanchoin, L. (2016). Architecture and connectivity govern actin network contractility. Curr. Biol. *26*, 616–626.
33. Wilde, A., and Zheng, Y. (1999). Stimulation of microtubule aster formation and spindle assembly by the small GTPase Ran. Science *284*, 1359–1362.
34. Farina, F., Gaillard, J., Guérin, C., Couté, Y., Sillibourne, J., Blanchoin, L., and Théry, M. (2016). The centrosome is an actin-organizing centre. Nat. Cell Biol. *18*, 65–75.
35. Wühr, M., Tan, E.S., Parker, S.K., Detrich, H.W., 3rd, and Mitchison, T.J. (2010). A model for cleavage plane determination in early amphibian and fish embryos. Curr. Biol. *20*, 2040–2045.
36. Cavazza, T., Peset, I., and Vernos, I. (2016). From meiosis to mitosis - the sperm centrosome defines the kinetics of spindle assembly after fertilization in Xenopus. J. Cell Sci. *129*, 2538–2547.
37. Wühr, M., Chen, Y., Dumont, S., Groen, A.C., Needleman, D.J., Salic, A., and Mitchison, T.J. (2008). Evidence for an upper limit to mitotic spindle length. Curr. Biol. *18*, 1256–1261.
38. Athale, C.A., Dinarina, A., Mora-Coral, M., Pugieux, C., Nedelec, F., and Karsenti, E. (2008). Regulation of microtubule dynamics by reaction cascades around chromosomes. Science *322*, 1243–1247.
39. Yokoyama, H., Gruss, O.J., Rybina, S., Caudron, M., Schelder, M., Wilm, M., Mattaj, I.W., and Karsenti, E. (2008). Cdk11 is a RanGTP-dependent microtubule stabilization factor that regulates spindle assembly rate. J. Cell Biol. *180*, 867–875.
40. Dogterom, M., and Bernard, Y. (1997). Measurement of the force-velocity relation for growing microtubules. Science *278*, 856–860.
41. Janson, M.E., de Dood, M.E., and Dogterom, M. (2003). Dynamic instability of microtubules is regulated by force. J. Cell Biol. *161*, 1029–1034.
42. Nejedla, M., Sadi, S., Sulimenko, V., de Almeida, F.N., Blom, H., Draber, P., Aspenström, P., and Karlsson, R. (2016). Profilin connects actin assembly with microtubule dynamics. Mol. Biol. Cell *27*, 2381–2393.
43. Applewhite, D.A., Grode, K.D., Keller, D., Zadeh, A.D., Slep, K.C., and Rogers, S.L. (2010). The spectraplakin Short stop is an actin-microtubule cross-linker that contributes to organization of the microtubule network. Mol. Biol. Cell *21*, 1714–1724.
44. MacKintosh, F.C., Käs, J., and Janmey, P.A. (1995). Elasticity of semiflexible biopolymer networks. Phys. Rev. Lett. *75*, 4425–4428.

45. Pujol, T., du Roure, O., Fermigier, M., and Heuvingh, J. (2012). Impact of branching on the elasticity of actin networks. Proc. Natl. Acad. Sci. USA *109*, 10364–10369.
46. Mogessie, B., and Schuh, M. (2017). Actin protects mammalian eggs against chromosome segregation errors. Science *357*, eaal1647.
47. Azoury, J., Lee, K.W., Georget, V., Hikal, P., and Verlhac, M.-H. (2011). Symmetry breaking in mouse oocytes requires transient F-actin meshwork destabilization. Development *138*, 2903–2908.
48. Field, C.M., Wühr, M., Anderson, G.A., Kueh, H.Y., Strickland, D., and Mitchison, T.J. (2011). Actin behavior in bulk cytoplasm is cell cycle regulated in early vertebrate embryos. J. Cell Sci. *124*, 2086–2095.
49. Isambert, H., Venier, P., Maggs, A.C., Fattoum, A., Kassab, R., Pantaloni, D., and Carlier, M.-F. (1995). Flexibility of actin filaments derived from thermal fluctuations. Effect of bound nucleotide, phalloidin, and muscle regulatory proteins. J. Biol. Chem. *270*, 11437–11444.
50. Reymann, A.-C., Martiel, J.-L., Cambier, T., Blanchoin, L., Boujemaa-Paterski, R., and Théry, M. (2010). Nucleation geometry governs ordered actin networks structures. Nat. Mater. *9*, 827–832.
51. Michelot, A., Berro, J., Guérin, C., Boujemaa-Paterski, R., Staiger, C.J., Martiel, J.L., and Blanchoin, L. (2007). Actin-filament stochastic dynamics mediated by ADF/cofilin. Curr. Biol. *17*, 825–833.
52. Izaurralde, E., Kutay, U., von Kobbe, C., Mattaj, I.W., and Görlich, D. (1997). The asymmetric distribution of the constituents of the Ran system is essential for transport into and out of the nucleus. EMBO J. *16*, 6535–6547.
53. Petry, S., Pugieux, C., Nédélec, F.J., and Vale, R.D. (2011). Augmin promotes meiotic spindle formation and bipolarity in Xenopus egg extracts. Proc. Natl. Acad. Sci. USA *108*, 14473–14478.
54. Hannak, E., and Heald, R. (2006). Investigating mitotic spindle assembly and function in vitro using Xenopus laevis egg extracts. Nat. Protoc. *1*, 2305–2314.
55. Gillespie, P.J., Gambus, A., and Blow, J.J. (2012). Preparation and use of Xenopus egg extracts to study DNA replication and chromatin associated proteins. Methods *57*, 203–213.
56. Shelanski, M.L. (1973). Chemistry of the filaments and tubules of brain. J. Histochem. Cytochem. *21*, 529–539.
57. Aumeier, C., Schaedel, L., Gaillard, J., John, K., Blanchoin, L., and Théry, M. (2016). Self-repair promotes microtubule rescue. Nat. Cell Biol. *18*, 1054–1064.
58. Machesky, L.M., Mullins, R.D., Higgs, H.N., Kaiser, D.A., Blanchoin, L., May, R.C., Hall, M.E., and Pollard, T.D. (1999). Scar, a WASp-related protein, activates nucleation of actin filaments by the Arp2/3 complex. Proc. Natl. Acad. Sci. USA *96*, 3739–3744.
59. Jimenez, A.M., Roché, M., Pinot, M., Panizza, P., Courbin, L., and Gueroui, Z. (2011). Towards high throughput production of artificial egg oocytes using microfluidics. Lab Chip *11*, 429–434.
60. de Chaumont, F., Dallongeville, S., Chenouard, N., Hervé, N., Pop, S., Provoost, T., Meas-Yedid, V., Pankajakshan, P., Lecomte, T., Le Montagner, Y., et al. (2012). Icy: an open bioimage informatics platform for extended reproducible research. Nat. Methods *9*, 690–696.
61. Tarantino, N., Tinevez, J.Y., Crowell, E.F., Boisson, B., Henriques, R., Mhlanga, M., Agou, F., Israël, A., and Laplantine, E. (2014). TNF and IL-1 exhibit distinct ubiquitin requirements for inducing NEMO-IKK supramolecular structures. J. Cell Biol. *204*, 231–245.
62. Valentine, M.T., Perlman, Z.E., Mitchison, T.J., and Weitz, D.A. (2005). Mechanical properties of Xenopus egg cytoplasmic extracts. Biophys. J. *88*, 680–689.
63. Achard, V., Martiel, J.L., Michelot, A., Guérin, C., Reymann, A.C., Blanchoin, L., and Boujemaa-Paterski, R. (2010). A "primer"-based mechanism underlies branched actin filament network formation and motility. Curr. Biol. *20*, 423–428.

# STAR★METHODS

## KEY RESOURCES TABLE

| REAGENT or RESOURCE | SOURCE | IDENTIFIER |
|---|---|---|
| Antibodies | | |
| NuMA-GFP | J. Pelletier and T.J Mitchison | N/A |
| Chemicals, Peptides, and Recombinant Proteins | | |
| HEPES | Sigma | H3375 |
| KCl | Sigma | P9333 |
| MgCl2 | Sigma | M8266 |
| EGTA | Sigma | E3889 |
| Sucrose | Sigma | S7903 |
| L-Cystein | Sigma | C7352 |
| DTT | Sigma | D0632 |
| Leupeptin | Sigma | L9783 |
| Pepstatin | Sigma | P5318 |
| Chymostatin | Sigma | C7268 |
| AEBSF | Sigma | A8456 |
| NaCl | Sigma | S7653 |
| ATP | Sigma | A7699 |
| Creatine phosphate | Sigma | P1937 |
| Creatine phosphokinase | Sigma | C3755 |
| Tubulin Porcine HiLyte 488 | Cytoskeleton | 027TL488M-A |
| Tubulin Porcine TRITC | Cytoskeleton | 027TL590MA |
| HiLyte Fluor 647 tubulin | Cytoskeleton | TL670M |
| Nocodazole | Sigma | M1404 |
| Mineral Oil | Sigma | M5904 |
| Arlacel P135 | UNIQEMA | N/A |
| Latrunculin-A | Sigma | L5163 |
| Blebbistatin | Sigma | B0560 |
| Alexa 488 | Life technology | A-20000 |
| Pipes | Sigma | P6757 |
| ATTO-565 | Atto Tec | AD565-31 |
| ATTO-488 | Atto Tec | AD488-31 |
| SiPEG 30 kDa | Creative PEGworks | PSB-2014 |
| SiPEG 5 kDa | Creative PEGworks | PLS-2011 |
| Neutravidin | Fischer Scientific | 10443985 |
| Actin | [49] | N/A |
| GST-WA | [50] | N/A |
| Arp2/3 | [51] | N/A |
| Latex fluorescent beads (0.1 um) | Life Technologies | F8803 |
| PLL(20 kDa) grafted with PEG(2 kDa) | Susos | PLL(20)-g[3.5]-PEG(2) |
| Experimental Models: Organisms/Strains | | |
| *Xenopus laevis* adulte female | *Xenopus* Express | http://www.xenopus.com |
| Recombinant DNA | | |
| RanQ69L | [52] | N/A |
| EB1-GFP | [53] | N/A |
| Utr-GFP | This study | N/A |
| Utr-dsRed | This study | N/A |

(*Continued on next page*)

*Continued*

| REAGENT or RESOURCE | SOURCE | IDENTIFIER |
|---|---|---|
| Software and Algorithms | | |
| SimplePCI | Hamamatsu | https://hcimage.com/simple-pci-legacy/ |
| Micro-Manager | Micro-Manager | https://micro-manager.org/wiki/Download%20Micro-Manager_Latest%20Release |
| Metamorph v7.7.5 | Molecular devices | https://www.moleculardevices.com/products/cellular-imaging-systems/acquisition-and-analysis-software/metamorph-microscopy |
| Fiji/ImageJ | ImageJ | https://imagej.net/Fiji/Downloads |
| MATLAB R2017b | Mathworks | https://www.mathworks.com/downloads/ |
| GraphPad Prism 6.0 | GraphPad Software | https://www.graphpad.com/scientific-software/ prism |

## CONTACT FOR REAGENT AND RESOURCE SHARING

Further information and requests for resources and reagents should be directed to and will be fulfilled by the Lead Contact, Zoher Gueroui (zoher.gueroui@ens.fr).

## EXPERIMENTAL MODEL AND SUBJECT DETAILS

### Actin-intact *Xenopus* egg extract preparation

*Xenopus laevis* egg extracts were prepared as previously described [26, 54]. ATP regenerating system (1 mM ATP, 10 mM creatine phosphate, 80 μg/mL creatine phosphokinase, final concentrations) was added at the beginning of each experiment. All reagents for buffer preparation were purchased from Sigma-Aldrich. Sperm nuclei were prepared as previously described [55]. Studies on *Xenopus leaves* have been approved by the committee "Comité National de Réflexion Ethique sur l'Expérimentation Animale - CE005" under the reference #755 2015060214546588 and all experiments were conform with the committee ethical rules.

## METHOD DETAILS

### Protein production and purification

Actin was purified from rabbit skeletal-muscle acetone powder and labeled with Alexa 488 according to the protocol described in [49]. Arp2/3 complex was purified as described earlier [51]. GST-WA (Arp2/3 activating domain of WASp) was expressed and purified as described previously [50]. Tubulin was purified from fresh bovine brain by three cycles of temperature-dependent assembly and/or disassembly in Brinkley Buffer 80 (BRB80 buffer: 80 mM Pipes pH 6.8, 1 mM EGTA and 1 mM $MgCl_2$) and labeled with ATTO-565 or ATTO-488 followed by the protocol described in [56]. Microtubule seeds were prepared with 20% ATTO-488-labeled tubulin and 80% biotinylated tubulin as described earlier [57].

Recombinant PWA (Scar-WA) proteins were produced as previously described [58]. RanQ69L, EB1-GFP, Utr-GFP, and Utr-dsRed were expressed from plasmids and purified using standard protocols.

### Microtubule nucleation and observation in *Xenopus* egg extracts

Microtubules were nucleated from several assembly pathways, mediated by sperm nuclei, centrosomes, or RanQ69L. Depending on the requirements of the experiments, microtubules were labeled with FITC-tubulin or HiLyte Fluor 647-tubulin (Cytoskeleton Inc.) at a final concentration of 300 nM or with EB1-GFP at a final concentration of 200 nM. The antibody NuMA-GFP was used at a final concentration of 7.5 μg/mL to characterize the spindle pole and was a gift of J.Pelletier and T.J.Mitchison. Asters nucleated from Ran were nucleated in the presence of 8 μM RanQ69L (final concentration). Unlabelled centrosomes were purified from Jurkat cells. Fluorescently labeled centrosomes were purified from HeLa cells expressing eGFP-centrin1.

Nocodazole was used to depolymerize microtubules at a final concentration of 10 μM in the extract.

### Generation of emulsion droplets/encapsulated extracts

Cell extract was encapsulated in droplets using a water-in-oil emulsion process. A biocompatible block copolymer (Arlacel P135) is added to mineral oil (Sigma) to stabilize emulsion and facilitate observations. This method, which has previously been described allows the formation of microtubule asters in droplets [59]. The *Xenopus laevis* egg extracts were added to the block copolymer solution (1% (v CSF/v Oil)) at room temperature. The mixture was then gently sheared by pipetting the solution up and down for a few seconds to generate extract-in-oil droplets. The mechanical dispersion of the biphasic solution formed micrometre-sized extract-in-oil droplets within a few seconds. The emulsion was incubated for 30 minutes at 19°C and then observed under the microscope for 45 minutes. The droplets presenting microtubule formation had a diameter comprised between 10 and 120 μm.

### Actin nucleation and observation in confined *Xenopus* extracts

Actin was labeled with GFP-Utrophin or dsRed-Utrophin at a final concentration of 80 nM. To impede F-actin meshwork formation, we treated the extract with Latrunculin-A (Sigma) and Blebbistatin (Sigma) at final concentrations of 25 μM and 70 μM, respectively. To promote homogeneous nucleation of F-actin in the droplets, PWA was used at final concentrations of 1.3 μM or 250 nM. The loose meshwork was obtained by PWA at a final concentration of 250 nM and Latrunculin-A at a final concentration of 4 μM.

### Bead coating

Beads introduced in the extract were coated with a polymer to avoid non-specific interactions with the intracellular environment. Latex fluorescent beads (0.1 μm, Life Technologies) were coated with 10 000 PLL-PEG (PLL(20)-g[3.5]-PEG(2), Susos) per particle. The coupling was done by electrostatic interaction between the poly-lysine of the PEG and the carboxyl groups on the surface of the particle.

### *In vitro* reconstitution of actin and microtubule networks

Microtubule and actin networks were reconstituted *in vitro* in a flow cell chamber with an approximate reaction volume of 30 μL with an entry and exit sites that were constructed using a double-sided tape (70 μm height) between a glass coverslip coated with (20% SiPEG-Biotin 30 kDa + 80% SiPEG 5kDa) and a passivated glass slide (SiPEG 30 kDa). Both the coverslip and glass slides were washed and coated with either SiPEG-Biotin / 30 kDa / 5 kDa prior to the experiment following a chemical cleaning procedure as described in [57]. For the microtubule control experiments, the biotynylated MT seeds were attached randomly on SiPEG (20% SiPEG-Biotin 30 KDa + 80% SiPEG 5kDa) coated coverslips by perfusing 100 ul of Neutravidin (0.05 mg $ml^{-1}$ in 1 X HKEM (10mM HEPES pH 7.5, 50 mM KCl, 5 mM $MgCl_2$, 1 mM EGTA)). The unbound seeds were washed away using 300 μL of wash buffer (1X HKEM supplemented with 0.1% BSA). Microtubules were elongated by introducing a mix of tubulin at 25 μM (20% labeled and 80% unlabelled tubulin) in TIC-TAC buffer (10 mM HEPES, 16 mM Pipes (pH 6.8), 50 mM KCl, 5 mM $MgCl_2$, 1 mM EGTA) supplemented with 1 mM GTP and 2.7 mM ATP, 10 mM DTT, 20 μg $ml^{-1}$ catalase, 3 mg $ml^{-1}$ glucose, 100 μg $ml^{-1}$ glucose oxidase and 0.25% w/v methylcellulose. The same experimental setup was followed to study actin-microtubule interaction, by the addition of Arp2/3 complex (50 nM), GST-WA (120 nM) and Actin (2 μM) for branched; Actin (2 μM) alone for unbranched network, in a 30 μL reaction.

### Imaging of Confined *Xenopus* extracts

Fluorescence imaging was performed using IX71 and IX81 Microscopes (Olympus) equipped with an EM-CCD camera (electron multiplying CCD, C9100-02, Hamamatsu, Corporation) or an ImageEM (X2 EM-CCD C9100-23B, Hamamatsu Corporation) respectively. An X60 (PlanApo, NA 1.42) oil objective and a LED system of illumination (Spectra X, Lumencor) were used. Microscope settings and functions were controlled using Simple PCI software (Hamamatsu) or Micro-Manager. Confocal microscopy was performed with a Zeiss LSM 710 META laser scanning confocal microscope using an X63 (PlanApochromatic, NA 1.4) objective. Image analysis was performed using ImageJ and MATLAB. The pole-to-chromosome distance was measured by taking the distance between the microtubule pole (maximum of fluorescence of the microtubule fluorescence channel) and the chromosome centroid.

Kymographs analysis: for branched contractile meshworks, we measured the F-actin velocity on movies with a 3 s interval whereas for the branched static meshwork, it was measured on movies with a 30 s interval (to obtain the necessary resolution for the velocity measurement). Kymographs were traced and analyzed with ImageJ software.

Quantitative analysis of EB1-GFP dynamics: movies were acquired with one image every second for one minute. Time projection of the movies allowed the measurement of microtubule length. Kymographs following the path of microtubules were traced and growth rate was extracted from those kymographs. For each condition described, two independent experiments were performed with two different cell extracts. In each experiment, three to six asters were monitored and analyzed.

Evaluation of EB1 count. To evaluate EB1 count, the comets were tracked with the ''Spot Detector'' plugin of Icy software. The coordinates were then used to compute the EB1 count as a function of the aster center.

Automated beads tracking was done with the software Icy [60]. The trajectories were obtained by using the Spot Tracking and the Track Manager Plugins. The trajectories were exported in Excel files and analyzed with MATLAB. The tracks were filtered to keep only the tracks with more than 30 points. Mean square displacement analysis was done with the msdanalyzer class in MATLAB [61]. Diffusion coefficient was computed from a linear fit on the first 25% of the curve. Alpha was computed from a linear fit on the first 25% of the log-log curve. Viscosity was computed as previously described [62].

For pole mobility, movies were acquired between 30 and 75 minutes after the beginning of the incubation. Droplets with only one pole were imaged at 30 s intervals for about 10-15 minutes. For movie analysis, tracking was done manually using the Manual Tracking plugin from ImageJ.

### Imaging of actin and microtubule networks *in vitro* by TIRF microscopy

Microtubules and actin were visualized on an inverted microscope using 60X Nikon APO TIRF oil-immersion objective. The microscope stage was maintained at 37 °C by means of a temperature controller to obtain an optimal microtubule growth. Excitation was achieved using lasers with wavelengths of 491 and 561 nm (Optical Insights). Multi-stage time-lapse movies were acquired using Metamorph software (version 7.7.5, Universal Imaging) with images taken every 5 s for 20 min. Movies obtained using Metamorph were further processed to improve the signal/noise ratio (Band pass filter and subtract background functions of ImageJ, version

1.47n5). The kymographs corresponding to the time-lapse movies (from 120 s to 860 s) were achieved using ImageJ. The microtubule dynamics were studied only at the plus end. The microtubule length presented in Figure 2D corresponds to the maximum length (μm) of the microtubule obtained from every MT seed analyzed during the time interval 120 s to 860 s. The apparent growth rate (μm/min) represents the maximum microtubule growth rate measured from every MT seed based on the kymograph analysis during the time interval 120 s to 860 s. The lifetime (s) represents the maximum time before which MTs undergo catastrophe. It is also measured for the same population of microtubules used for length measurements, during the same time interval 120 s to 860 s. Catastrophe events were calculated from kymographs obtained with ImageJ, corresponding to the MTs originating from every MT seed under different conditions over the time interval 120 s to 860 s. Number of catastrophe events were obtained by counting the number of catastrophes per kymograph. The growth of actin branched network is never fully homogeneous due to primer activation [63]. Indeed, the formation of a branched network is an autocatalytic process emanating from an initial filament (name primer or mother filament); this process generates part of the reaction chamber with a dense actin network where other parts are deprived of network. Therefore, some microtubule seeds are embedded in the branched actin network and some never embedded. We used the first population to determine the role of a branched actin network on microtubule dynamics and the second population, as an internal control to demonstrate that actin monomers, pWA or Arp2/3 complex did not have any effect on microtubule dynamics. This population is represented as "absence of surrounding actin network" in Figures 2F, 2G, and 2I. The corresponding graphs were produced using GraphPad Prism 6.0.

## QUANTIFICATION AND STATISTICAL ANALYSIS

### Data analysis of Confined *Xenopus* extracts

Data treatment was performed with Excel and MATLAB. Student's t tests were performed with MATLAB. For the interpretation of the p values, NS means there is no significant difference between the two distributions. One star means p value $< 0.05$, two stars means p value $< 0.01$, and three stars means p value $< 0.001$. Error bars always show the standard deviation. For each condition, at least three independent experiments were done.

### Data analysis of *in vitro* actin and microtubule networks

Statistical analysis were obtained using Mann-Witney test assuming non-paired and non-Gaussian distribution.